LIMNOLOGY and OCEANOGRAPHY

ASLO

Limnol. Oceanogr. 9999, 2023, 1–18

doi: 10.1002/lno.12404

Distinct habitat and biogeochemical properties of low-oxygen-adapted tropical oceanic phytoplankton

Isabelle Cox,[1] Robert J. W. Brewin ,[1*] Giorgio Dall'Olmo,[2,3] Katy Sheen,[1] Shubha Sathyendranath,[3] Rafael Rasse,[4] Osvaldo Ulloa [5,6]

[1]Centre for Geography and Environmental Science, Department of Earth and Environmental Science, Faculty of Environment, Science and Economy, University of Exeter, Cornwall, UK
[2]National Institute of Oceanography and Applied Geophysics–OGS, Trieste, Italy
[3]National Centre for Earth Observation, Plymouth Marine Laboratory, Plymouth, UK
[4]Sorbonne Universités, UPMC Université Paris 06, CNRS, Laboratoire d'Océanographie de Villefranche (LOV) UMR7093, Observatoire Océanologique, Villefranche-sur-Mer, France
[5]Department of Oceanography, Universidad de Concepción, Concepción, Chile
[6]Millennium Institute of Oceanography, Universidad de Concepción, Concepción, Chile

Abstract

We use data collected by Biogeochemical Argo (BGC-Argo) float, over a 5-year period (2016–2021), to study the dynamics of a unique low-oxygen-adapted phytoplanktonic community in the eastern tropical North Pacific. We isolate this community using a model that partitions vertical profiles of chlorophyll *a* (Chl *a*) and particulate backscattering into the contributions of three communities of phytoplankton: C_1, the community in the mixed-layer; C_2, at the deep Chl *a* maximum; and C_3, in low-oxygen waters at the base of the euphotic zone. We find that C_3 has a similar chl-specific particulate backscattering to C_2, both lower than C_1. C_2 and C_3 contribute significantly to integrated stocks of Chl *a*, both at around 41%, and both around 30% of integrated particulate backscattering (after removing a background signal attributed to nonalgal particles). Found at depths of around 100 m, the peak biomass of C_3 is lower than C_2 (located at around 60 m), and yet, C_3 makes similar contributions to integrated stocks, because it has a broader peak than C_2. In relation to C_1 and C_2, C_3 thrives in a lower temperature, higher density, lower light, lower oxygen, and higher saline habitat. This work illustrates how BGC-Argo floats, in combination with simple conceptual models, can be used to observe the dynamics of unique communities of phytoplankton in extreme environments. The projected climate-driven changes in oxygen minimum zones add urgency to understand the vulnerabilities of these communities both in terms of stocks and composition.

Phytoplankton are photosynthesizing, microscopic, unicellular algae that occupy the euphotic zone (Reynolds 2006). Extracting energy from light through photosynthesis and converting inorganic carbon (carbon dioxide) into organic carbon, phytoplankton contribute to around 50% of global net primary production (Longhurst et al. 1995; Field et al. 1998). They modify the total CO_2 concentration within the upper ocean, impacting the air-sea CO_2 flux that regulates Earth's climate (Falkowski 2012). Energy produced by phytoplankton—in the form of organic carbon—is made available to most of the marine ecosystem, sustaining mesopelagic and bathypelagic communities (Reynolds 2006; Martiny et al. 2022). Phytoplankton are considered an essential climate variable (GCOS 2011), imperative to the ocean's biological pump—one of the Earth's major carbon sinks (Basu and Mackey 2018; Brewin et al. 2021). Produced particulate organic carbon (POC) is consumed and processed by microbes, zooplankton, and subsequent trophic levels, and later respired back into inorganic carbon, or transferred into the deep ocean (Basu and Mackey 2018), a process referred to as the biological pump. The efficiency of the biological pump and the amount of

*Correspondence: r.brewin@exeter.ac.uk

Additional Supporting Information may be found in the online version of this article.

Author Contribution Statement: R.J.W.B. and I.C. designed the study and performed the analysis. G.D. and R.R. were responsible for data collection and the deployment of the BGC-Argo float. G.D., K.S., S.S., and O.U. guided the analysis. I.C. wrote the draft with input from R.J.W.B. All authors edited subsequent versions of the manuscript and approved the final submission.

organic carbon produced at the surface that is transferred to the deep ocean, is dependent on phytoplanktonic physiology, community structure and species dynamics, distribution, and vertical structure, as governed by environmental conditions (Basu and Mackey 2018). Distinct communities and species of phytoplankton also contribute differently to the cycling of biogeochemical elements other than carbon, such as the nitrogen, silica, iron, and phosphate cycles (Arrigo 2005; Le Quéré et al. 2005; IOCCG 2014), maintaining planetary homeostasis.

Elevated concentrations of phytoplankton are typically found in regions where nutrient concentrations are high—including coastal regions and upwelling regions, and, during spring in temperate and high latitudes—while lower concentrations are often associated with the central oligotrophic gyres that are governed by nutrient limitation (Longhurst et al. 1995). Comprised of an estimated ~ 25,000 species (Marañón 2009), phytoplankton have adapted to thrive in a wide variety of environments, occupying a range of environmental niches. Examples include the high-light, shallow mixed layer of the tropical ocean, the very low-light, deep mixed layer of high latitudes during winter, and more extreme habitats such as under sea ice and in oxygen minimum zones (OMZs). Phytoplankton have been observed at the base of the euphotic zone in OMZs (Goericke et al. 2000; Cepeda-Morales et al. 2009; Whitmire et al. 2009), where light is limiting to phytoplanktonic growth. Found in regions of strong stratification, subsurface low-oxygen zones occur due to the decomposition of surface-derived sinking organic material by aerobic respiration (Ulloa et al. 2012; Long et al. 2019). OMZs are projected to expand by 2100 (International Panel on Climate Change, IPCC 2018). In some cases, these oxygen-depleted waters—which can be rich in nutrients—intrude into the base of the euphotic zone, establishing a habitat for phytoplanktonic growth (Cepeda-Morales et al. 2009; Fuchsman et al. 2019).

Previous studies (e.g., Goericke et al. 2000; Lavin et al. 2010) have outlined the physiological and genetic adaptivity of phytoplanktonic cells that can grow and thrive in these extreme low-light and low-oxygen environments. They have shown that the community found in these environments is composed of the cyanobacteria *Prochlorococcus* and *Synechococcus* (Goericke et al. 2000; Lavin et al. 2010). The dominant abundance of *Prochlorococcus* at the bottom of the euphotic zone is attributed to its physiological plasticity and genetic diversity. *Prochlorococcus*—composed of at least 12 distinct lineages—can be divided into high- and low-light adapted ecotypes (Bouman et al. 2006; Biller et al. 2015). Goericke et al. (2000) and Lavin et al. (2010) have shown some low-light lineages to have a competitive advantage in low-oxygen environments below the euphotic depth. Dominance of *Prochlorococcus* in oxygen-depleted waters has been attributed to species emergence in low-oxygen conditions in the ancient ocean, with lineages retaining phycobilisomes as light-harvesting antennae, contributing to their ability to sustain aerobic metabolisms in oxygen-depleted waters (Ulloa et al. 2021). *Synechococcus* are also reported to reside in the low-light, low-oxygen conditions (Goericke et al. 2000; Lavin et al. 2010) along with *Prochlorococcus*. However, their concentrations appear consistently lower than those of *Prochlorococcus* within the OMZ (Goericke et al. 2000; Lavin et al. 2010).

The niche that the low-oxygen, low-light phytoplankton occupy makes it difficult to observe these phytoplankton. Satellite remote sensing of ocean color is recognized as an important tool to monitoring phytoplankton (Moisan et al. 2017; Sathyendranath et al. 2019; Brewin et al. 2022). The capability to monitor phytoplankton abundance on global and synoptic scales allows for an assessment of the entire global surface phytoplankton distribution and abundance (Gordon et al. 1980; Groom et al. 2019). Although effective at representing the ocean surface (< 30 m), satellites are unable to observe phytoplankton abundance within stratified regions at depths of 50–200 m (Brewin et al. 2022). Monitoring phytoplankton communities below the surface layer in these seasonally and permanently stratified regions (that constitute ~ 70% of the global ocean) requires in-situ measurements. Although important for studying phytoplankton at deeper depths of the water column, traditional ship-based monitoring cannot provide the high spatial and temporal coverage needed to improve our understanding phytoplankton dynamics and distributions at depth. This is now possible, however, using ocean robotic platforms, such as autonomous profiling floats (Chai et al. 2020; Claustre et al. 2020).

Autonomous profiling floats, including Biogeochemical Argo floats (BGC-Argo floats), are designed to explore the biogeochemical and physical dynamics of the ocean up to depths of 2000 m, collecting data at higher spatial and temporal resolutions than conventical platforms (Ravichandran et al. 2012; Bittig et al. 2019). Alongside collecting environmental data, BGC-Argo floats have optical sensors measuring chlorophyll *a* (Chl *a*) pigment concentration and particulate backscattering (b_{bp}), both of which have been used as measures of phytoplanktonic biomass (Martiny et al. 2022). Brewin et al. (2022) used a conceptual model to partition vertical profiles of Chl *a* and b_{bp}, collected using a BGC-Argo float in the northern Red Sea, into the contributions of two phytoplanktonic communities (C_1 in the surface mixed layer, and C_2 at the deep chlorophyll maximum), to examine their seasonal dynamics.

Here, the two-community model of Brewin et al. (2022) is extended by adding a third community that thrives in low-oxygen, low-light waters at the base of the euphotic zone. By applying the model to data collected by a BGC-Argo float in the eastern tropical North Pacific (ETNP) over a 5-year period (2016–2021), we explore the environmental niche and dynamics of this unique third phytoplanktonic community. Specifically, this work has the following aims: (1) Quantify the vertical structure of the third phytoplanktonic community, with respect to other communities in the water column; (2) Use a combination of Chl *a* and b_{bp} data to characterize

the third phytoplanktonic community; (3) Assess the contribution of the low-oxygen-adapted community to the stocks of phytoplankton (inferred from Chl *a* and b_{bp}) in the water column, and compare these to other phytoplankton communities within the water column; and (4) Quantify the environmental conditions in which the low-oxygen-adapted community thrives, and how these environmental conditions contrast to those where other communities are found.

Methods

Study area

Located between 9.8°N–14.5°N, 118°W–108°W, the study area is situated in the eastern tropical North Pacific Ocean (ETNP, Fig. 1). This region is characterized by reduced seasonal variation, sluggish circulation, and weak internal mixing (Fiedler and Talley 2006). The study area is influenced by a strong interannual climate variability, with the El Niño-Southern Oscillation (ENSO) dominating this interannual variability (Timmermann and Jin 2002). The amalgamation of high surface phytoplanktonic productivity, sinking organic matter, strong stratification, ENSO, the Pacific Decadal Oscillation, and the resultant reduced mixing and sluggish circulation, generates extensive subsurface oxygen depletion (Tiano et al. 2014; Duteil et al. 2018). Home to Earth's largest OMZ, the imbalance between supply and demand of oxygen in the OMZ below depths of 100 m has led to the development of an environment that supports the presence of unique planktonic communities (Cepeda-Morales et al. 2009; Stramma et al. 2010; Lam and Kuypers 2011; Fenchel et al. 2012; Long et al. 2019).

Biogeochemical Argo float (WMO 3901531)

Data in this study were collected using a *PROVOR* BGC-Argo float (Argo 2000) in the ETNP along the geographical locations displayed in Fig. 1 (World Meteorological Organization [WMO] number 3901531), downloaded from the Ifremer Argo data assembly centre (ftp://ftp.ifremer.fr/ifremer/argo/dac/bodc/; Sprof file). Equipped with conductivity-temperature-depth (CTD) sensors, dissolved oxygen (DO) optode, downwelling irradiance radiometer (at wavelengths of 380, 412, and 490 nm) alongside a photosynthetically active radiation (PAR) radiometer, chlorophyll-a fluorometer (Chl *a*), backscattering meter (b_{bp}), and an iridium transmission system (GPS), the BGC-Argo provides data from which profiles of temperature (°C), salinity (PSU), DO (μmol kg^{-1}), Chl *a* (mg m^{-3}), b_{bp} (m^{-1}), and PAR (mol quanta m^{-2} d^{-1}) were measured. Pressure, temperature, PAR, and salinity data were delayed-mode quality-controlled. For each profile, density (kg m^{-3}) and the Brunt-Väisälä buoyancy frequency (N^2 in units of s^{-2}, where N is computed as radians per second), were computed using the Python seawater package (version 3.3). The mixed layer depth (Z_m) was computed using Holte and Talley (2009) method for each profile, using the temperature algorithm (Python package https://github.com/garrettdreyfus/python-holteandtalley). For Chl *a* (Adjusted mode), DO and b_{bp} profiles (both real-time mode) additional processing steps (as described by Schmechtig et al. 2018, 2019) were employed to ensure maximum data quality. The adjusted mode Chl *a* data were processed as follows: the fluorescence measurements were first corrected by subtracting a dark fluorescence value; the dark-corrected fluorescence values were then multiplied by the manufacturers scaling factor to convert to a Chl *a* concentration and divided by two following recommendations by Roesler et al. (2017) who found a systematic overestimate of Chl *a* by a factor of two when testing WET Labs ECO sensors; the range of Chl *a* in the profile was then checked for realistic values (should be between −0.1 and 50 mg m^{-3}) and the profile was tested for negative Chl *a* spikes; and finally the profile was checked for nonphotochemical quenching (NPQ) on Chl *a* and if required, corrected based on a method adapted from Xing et al. (2012). Schmechtig et al. (2018) provides further details on the Chl *a* processing.

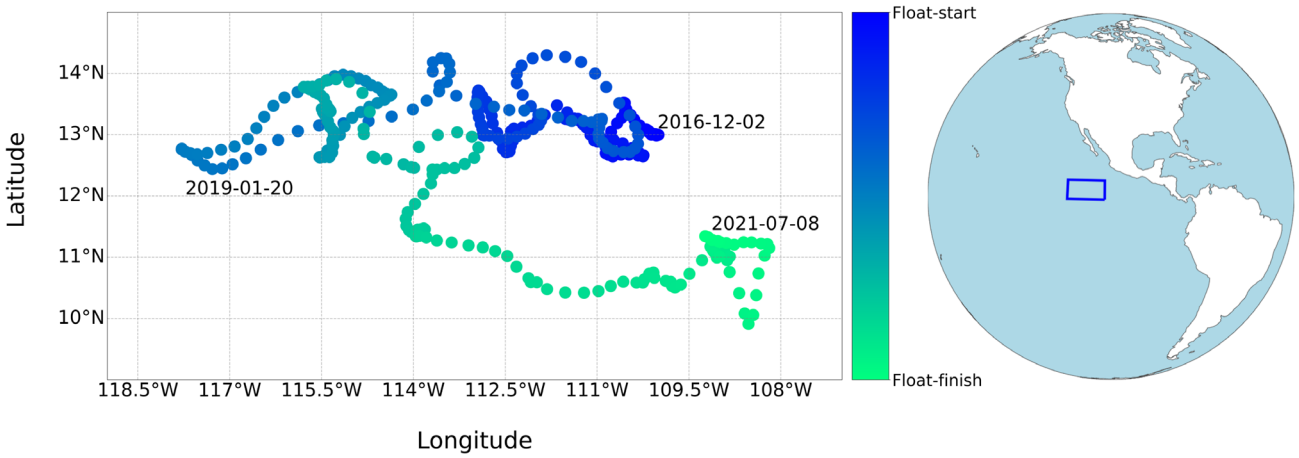

Fig. 1. Map of WMO 3901531 float trajectory.

Instantaneous measurements of PAR were converted into daily integrals following Brewin et al. (2022), accounting for day length as a function of the time of year and latitude, and under the assumption of a sinusoidal light cycle (Brewin et al. 2020). The diffuse attenuation coefficient (K_d), representing the attenuation of PAR with depth, was computed for each profile by fitting a Beer–Lambert law to the PAR data in the top 200 m of the water column (Brewin et al. 2022). Profiles where K_d could not be computed were removed.

Three-community model development

For this study, the two-community model of Brewin et al. (2022) was extended into a three-community model. First, and for a Chl *a* given profile, the dimensionless optical depth (τ) was computed by multiplying the geometric depth (m) by K_d (m^{-1}). Following Brewin et al. (2022), the Chl *a* profile was then converted into a normalized profile (B^*), in which the Chl *a* concentration (B) at depth (z) was divided by the surface Chl *a* concentration (B_s), taken as the median Chl *a* in the first optical depth. This was conducted after the removal of profiles without surface Chl *a*, profiles with less than 11 measurments, or with surface Chl *a* values $<0.01\,mg\,m^{-3}$. The normalized Chl *a* concentration (B^*) at a particular optical depth (τ) was then considered as a combination of contributions from three communities of phytoplankton.

Community 1 represents as a group of phytoplanktonic species that principally dwell in the turbulent mixed layer in the surface ocean, and following Brewin et al. (2022), was expressed as,

$$B_1^*(\tau) = 1 - \frac{1}{1+\exp\left[-\frac{P_1}{\tau_1}(\tau-\tau_1)\right]}, \quad (1)$$

where, P_1 controls the slope of change in B_1^* with τ, and τ_1 represents the midpoint of the slope (Brewin et al. 2022). It was assumed that as τ tends to zero, community 1 would dominate the surface Chl *a* concentration (>99%).

Community 2 represents the group of phytoplanktonic species that resides in a stable environment below the mixed layer, characteristic of the phytoplanktonic community at the first deep Chl *a* maximum (DCM1). Following Brewin et al. (2022), B_2^* was modeled as a Gaussian function of τ, such that,

$$B_2^*(\tau) = B_{m,2}^* \exp\left[-\left(\frac{\tau-\tau_2}{\sigma_2}\right)^2\right], \quad (2)$$

where $B_{m,2}^*$ defines the maximum value of the DCM1 (B_2^*), the dimensionless depth where $B_{m,2}^*$ occurs is τ_2, and the width of the $B_{m,2}^*$ peak is defined by σ_2.

Community 3 represents the phytoplanktonic group beneath community 2, living in very low-light and low-oxygen conditions (*see* Goericke et al. 2000; Márquez-Artavia et al. 2019). Similarly, B_3^* is modeled as a Gaussian function of τ, such that,

$$B_3^*(\tau) = B_{m,3}^* \exp\left[-\left(\frac{\tau-\tau_3}{\sigma_3}\right)^2\right], \quad (3)$$

where $B_{m,3}^*$ represents the maximum value of the second DCM (B_3^*); the dimensionless depth where $B_{m,3}^*$ occurs is τ_3, and the width of the $B_{m,3}^*$ peak is defined by σ_3.

Communities 1, 2, and 3 (Eqs. 1–3) can be combined to derive the total normalized chlorophyll profile (B^*), expressed as,

$$B^*(\tau) = 1 - \frac{1}{1+\exp\left[-\frac{P_1}{\tau_1}(\tau-\tau_1)\right]} + B_{m,2}^* \exp\left[-\left(\frac{\tau-\tau_2}{\sigma_2}\right)^2\right] + B_{m,3}^* \exp\left[-\left(\frac{\tau-\tau_3}{\sigma_3}\right)^2\right]. \quad (4)$$

The total Chl *a* concentration (B) at depth (z) can be reconstructed by scaling to B_s and K_d, with knowledge of the eight parameters: P_1, τ_1, $B_{m,2}^*$, τ_2, σ_2, $B_{m,3}^*$, τ_3, and σ_3.

Owing to strong stratification in the region, the model parameters were independently derived for each profile, as follows. First, parameters P_1 and τ_1, which are physical and optical in nature, were estimated empirically from Z_m and K_d following Brewin et al. (2022), where $\tau_1 = 0.62\ Z_m K_d + 2.29$ and $P_1 = 10^{0.08\tau_1+0.06}$. Once τ_1 and P_1 are known (and fixed), the other parameters $B_{m,2}^*$, τ_2, $B_{m,3}^*$, τ_3, and σ_3 are estimated by fitting the chlorophyll model to the data. The optimization function used was Levenberg–Marquardt iterative minimization (Python function minimize). Initial guesses of parameters were as follows: σ_2 and σ_3 were set to one, while $B_{m,2}^*$ and $B_{m,3}^*$ were initialised by extracting the maximum B^* above and below $5\,\mu mol\,kg^{-1}$ DO depth, and τ_2 and τ_3 were initialised at the depths of these respective maximums. Once model parameters were obtained, Chl *a* profiles were reconstructed by scaling the normalized profiles by B_s and K_d.

Following Brewin et al. (2022), the model was further extended to reproduce profiles of particle backscattering at 700 nm (b_{bp}), in the top 300 m of the water column. To do this, first b_{bp} is normalized by the surface particle backscattering ($b_{bp,s}$) defined as the median b_{bp} within the first optical depth. The normalized particle backscattering (b_{bp}^*) at a given optical depth (τ) is then considered as a combination of the three phytoplanktonic communities and a background component, attributed primarily to nonalgal particles, such that,

$$b_{bp}^*(\tau) = \omega_1 B_1^*(\tau) + \omega_2 B_2^*(\tau) + \omega_3 B_3^*(\tau) + b_{bp,k}^*, \quad (5)$$

where scaling factors, ω_1, ω_2, and ω_3, link the three phytoplanktonic communities ($B_1^*(\tau)$, $B_2^*(\tau)$, and $B_3^*(\tau)$) to particle backscattering, and $b_{bp,k}^*$ is a constant background factor

(Brewin et al. 2012). Assuming that ω_1 can be expressed as $1 - b^*_{bp,k}$ as in Brewin et al. (2022), the backscattering model can be further simplified, such that,

$$b^*_{bp}(\tau) = \left(1 - b^*_{bp,k}\right) B^*_1(\tau) + \omega_2 B^*_2(\tau) + \omega_3 B^*_3(\tau) + b^*_{bp,k}. \quad (6)$$

Having quantified $B^*_1(\tau)$, $B^*_2(\tau)$, and $B^*_3(\tau)$, the parameters ω_2, ω_3, and $b^*_{bp,k}$ required for the backscattering model were computed by fitting Eq. 6 to b_{bp} profiles using the Levenberg–Marquardt method (python function minimize). Initial guesses for ω_2, ω_3, and $b^*_{bp,k}$ were set to 0.3, 0.3, and 0.8, respectively, and constrained to a lower limit of 0.05 and upper limit of 0.95, as with Brewin et al. (2022). Chlorophyll-specific particulate backscattering coefficients, $b^B_{bp,1}$, $b^B_{bp,2}$, and $b^B_{bp,3}$, were then derived once ω_2 and $b^*_{bp,k}$ were known, by dividing the scaling factors—ω_1, ω_2, and ω_3—by the ratio of surface Chl *a* and surface particle backscattering ($B_s/b_{bp,s}$). The background particle backscattering coefficient (b^k_{bp})—thought to be dominated by nonalgal particles in the Pacific (Zhang et al. 2020)—was computed by multiplying $b^*_{bp,k}$ by surface particle backscattering ($b_{bp,s}$). Once model parameters were known, the particulate backscattering profiles were also reconstructed by rescaling the normalized profiles by surface particle backscattering ($b_{bp,s}$) and K_d. Backscattering profiles were apparently compromised (owing possibly to debris attached to the sensor) in mid 2018, returning to realistic values by late 2018. The compromised data were excluded from the analysis. An example of a model fit to a profile from the float is displayed in Fig. 2. The trapezoid method was used to carry out depth integration in the upper 200 m of the water column.

Extraction of environmental data for the three communities

Environmental conditions where the three communities were present (temperature, salinity, density, Brunt-Väisälä, DO, and PAR) were extracted for each BGC-Argo profile. For community 1 (C_1), median values in the mixed layer were computed. Meanwhile, for community 2 (C_2) and 3 (C_3), environmental data at τ_2 and τ_3 were used, respectively. Data from all profiles were combined and used to evaluate the habitats that the communities reside in.

Results

Performance and fit of model

The three-community Chl *a* model is seen to successfully capture the dynamics and trends of the BGC-Argo float data (Fig. 3a,b). Differences between in situ and modeled data are close to zero across large areas of the water column (median difference = −0.003 mg m^{-3}, standard deviation = 0.03 mg m^{-3}; Fig. 3c, *see* Supporting Information Fig. S1 for percentage deviations between model and data), in some cases higher, for instances where the model fails to represent the complexity of the Chl *a* profile. The contributions of the three communities (C_1 community 1; C_2 community 2; and C_3 community 3) to the Chl *a* profiles are displayed in Fig. 3d–f, with C_1 dominating the mixed layer and having higher concentrations during the winter (November to April). The presence of C_2 is fairly constant over the annual cycle, with the depth of the peak biomass found at around 60 m, fluctuating between 40 and 100 m, being shallower in the winter months due to lower surface light availability (Fig. 3e, Supporting Information Figs. S2, S3). In contrast to C_2, C_3 thrives below the 5 μmol kg^{-1} DO boundary, having a peak biomass depth at around 100 m, with some fluctuations between 50 and 200 m, deepening during the spring and summer. Additionally, the three-community model is found to successfully replicate the bulk backscattering fields (Fig. 4), but with a slight tendency to overestimate around the two DCMs, and slightly underestimate above and below the depth ranges, with a median difference of 0.00007 m^{-1} (standard deviation 0.00012 m^{-1}, *see* Supporting Information Fig. S1 for percentage deviations between model and data).

Parameters of communities 2 and 3

Considering the identical mathematical expressions for C_2 and C_3 (Eqs. 2 and 3), the parameters of the two communities can be cross compared (Fig. 5). We see that C_2 has a median peak value of 0.49 mg m^{-3} ($B^*_{2,m} \times B_S$), a median width of peak of 13.2 m (σ_2/K_d) and a depth of peak of 60.8 m (t_2/K_d), whereas C_3 has a deeper median depth of peak of 106.4 m (t_3/K_d), and a lower median peak value of 0.30 mg m^{-3} ($B^*_{3,m} \times B_S$) when compared with C_2, but a greater median peak width of 24.7 (σ_3/K_d). The parameters of the two communities remain different over the course of the year but show some seasonal variability (see Supporting Information Fig. S3). For example, with maximum peak values, and maximum depth of peaks, for both communities (C_2 and C_3) in spring, and minimums in winter (Supporting Information Fig. S3).

Contributions to community stocks

The chlorophyll-specific particulate backscattering coefficient is highest for C_1, with a median value of 0.006 m^2 [mg B]$^{-1}$. Both C_2 and C_3 have very similar chlorophyll-specific particulate backscattering coefficients, with C_3 having a slightly higher value than C_2, of 0.0010 m^2 [mg B]$^{-1}$ (standard deviation = 0.0006) and 0.0009 m^2[mg B]$^{-1}$ (standard deviation = 0.0007) respectively (Fig. 6a). The background backscattering coefficient (b^k_{bp}) has a median value of 0.0004 m^{-1}. Background backscattering dominates b_{bp} contributing 61% to the integrated particulate backscattering (Fig. 6b). The populations C_2 and C_3 contribute similarly to integrated particulate backscattering, with C_3 contributing 0.7% more than C_2 (10.0% and 10.7%, respectively), though the difference is not statistically significant. When removing the background backscattering coefficient from integrated particulate backscattering, C_1

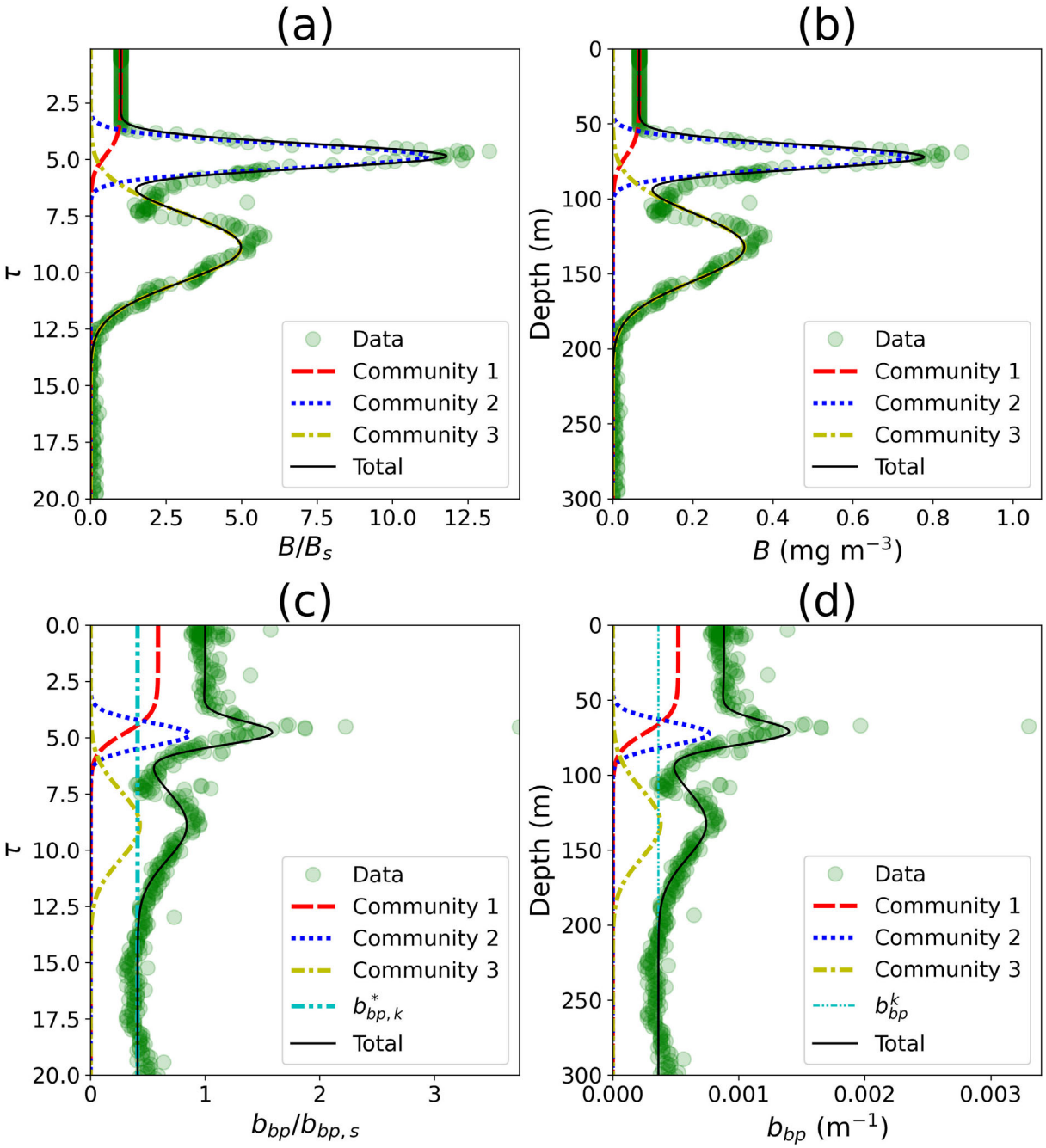

Fig. 2. An example fit (profile collected on 04 June 2017) of the (**a**) scaled dimensionless variables of chlorophyll *a*, (**b**) rescaled fields in absolute units for chlorophyll *a*, (**c**) scaled dimensionless variables of particulate backscattering, and (**d**) rescaled fields in absolute units for particulate backscattering models.

remains the highest contributor to particulate backscattering with a median of 41%. The median contribution of C_3 is slightly greater than C_2 (27% and 26%, respectively). However, the interquartile range for C_2 overlaps with C_3 (Fig. 6c) indicating no significance in differences between these two communities.

In contrast to the high contribution of C_1 to particulate backscattering, the median value of the contribution of C_1 to integrated Chl *a* is low, at around 11%, though there are occasional profiles in which C_1 dominates, contributing up to ~ 99% integrated Chl *a* (see outliers in Fig. 6d). Like the patterns identified in Fig. 6a–c, the contributions to integrated Chl *a* by C_2 and C_3

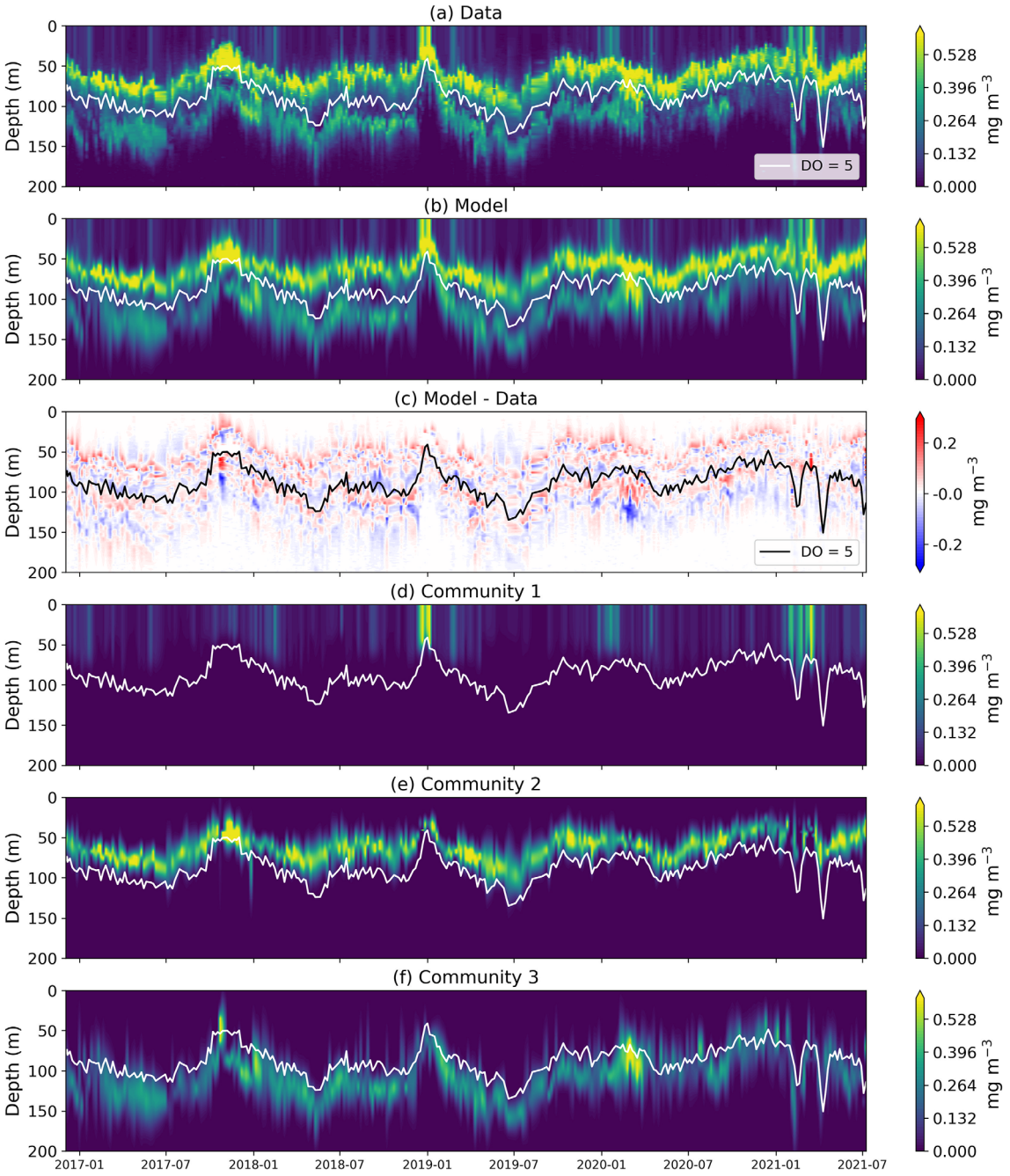

Fig. 3. Contour plots of the Chl *a* concentrations collected by the BGC-Argo float between 02 December 2016 and 08 July 2021 in the top 200 m of the water column. (**a**) Total Chl *a* data extracted from the BGC-Argo float, (**b**) parameterized and tuned model output of the total Chl *a*, (**c**) differences between the total Chl *a* model output and data, (**d**) model output for C_1, (**e**) model output for C_2, and (**f**) model output for C_3. White line (black line in subplot c) represents the depth where DO falls below 5 μmol kg^{-1}.

are statistically similar, with median values of 44% and 41%, respectively.

Environmental niches for the three communities

Temperature

Thriving at differing depths, the thermal niche of each community drastically differs (Fig. 7a). Heat uptake by seawater is highest at the surface due to the absorption of solar radiation (Whitmarsh et al., 2015). Therefore, as expected, C_1 resides in waters with the highest temperature (median 28.2°C). As temperature decreases with depth, C_2 and C_3 are associated with lower temperatures, with C_2 located above the thermocline (see Supporting Information Fig. S2), thriving in slightly cooler waters than C_1 (median

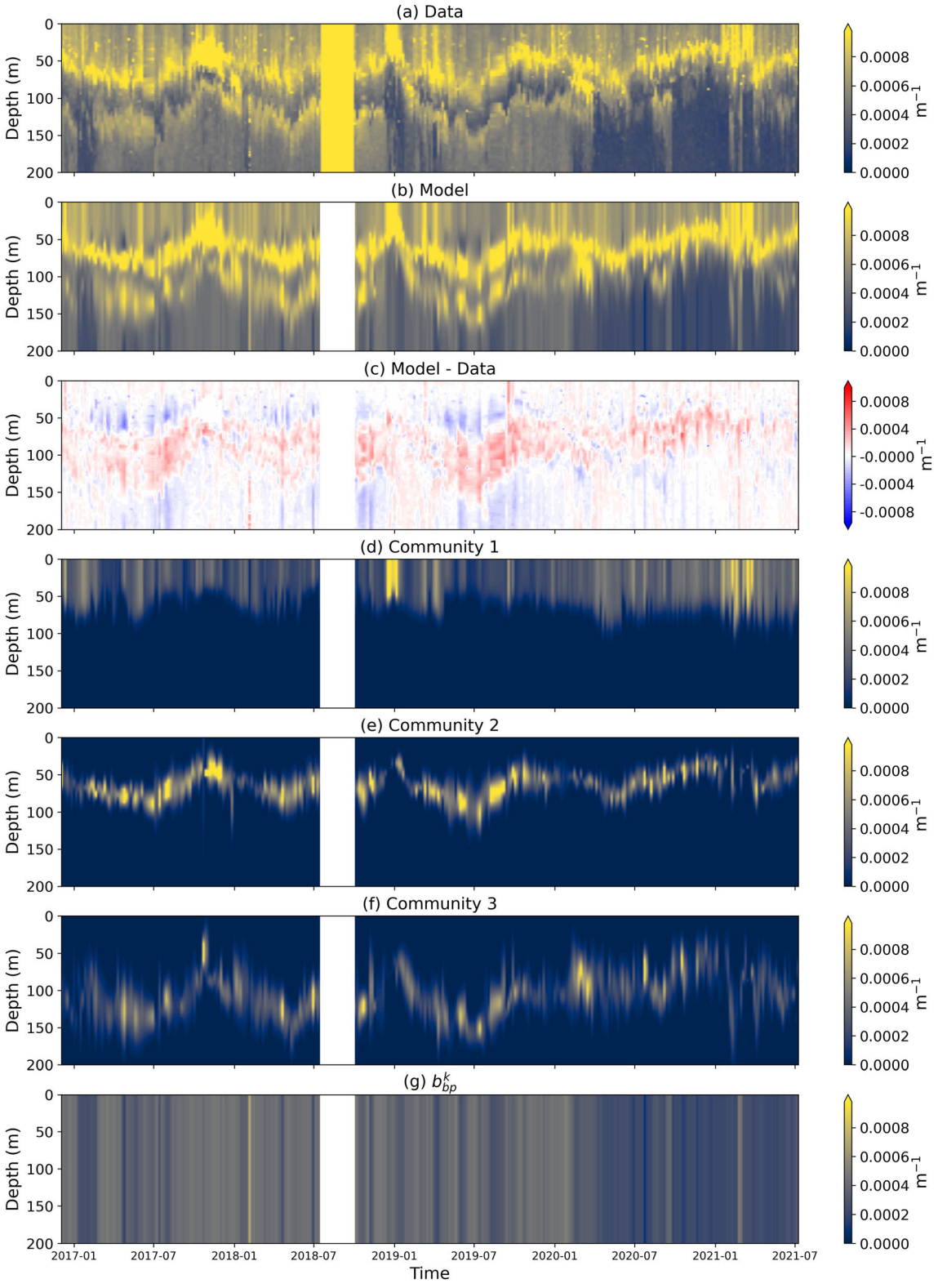

Fig. 4. Contour plots of b_{bp} taken from the BGC-Argo float between 02 December 2016 and 08 July 2021 throughout the top 200 m of the water column. (**a**) Total b_{bp} data extracted from the BGC-Argo float, (**b**) parameterized and tuned model output of the total b_{bp}, (**c**) differences between the total b_{bp} model output and data, (**d**) model output for C_1, (**e**) model output for C_2, (**f**) model output for C_3, and (**g**) background backscattering (b_{bp}^{k}).

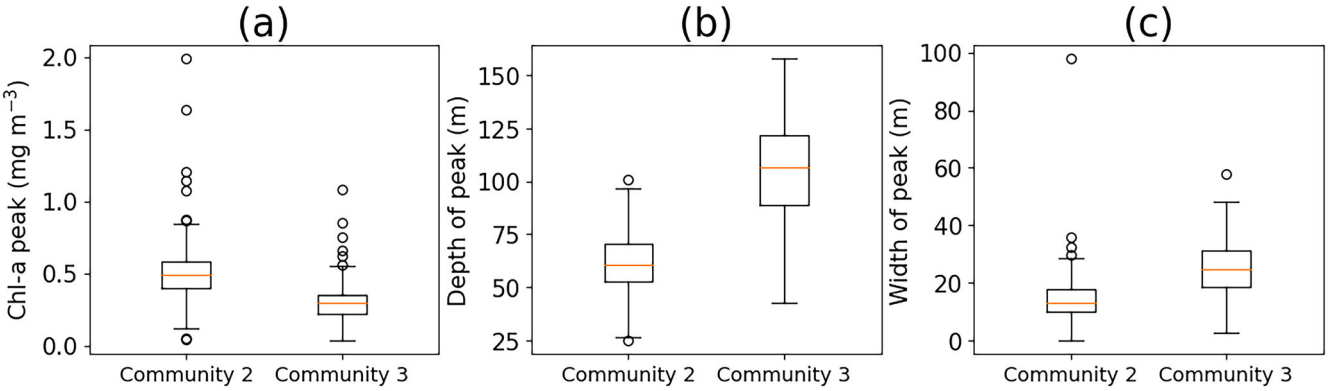

Fig. 5. Boxplots of the (**a**) Chl *a* peaks, (**b**) depth of Chl *a* peaks, and (**c**) width of Chl *a* peaks, for community 2 (C_2) and community 3 (C_3).

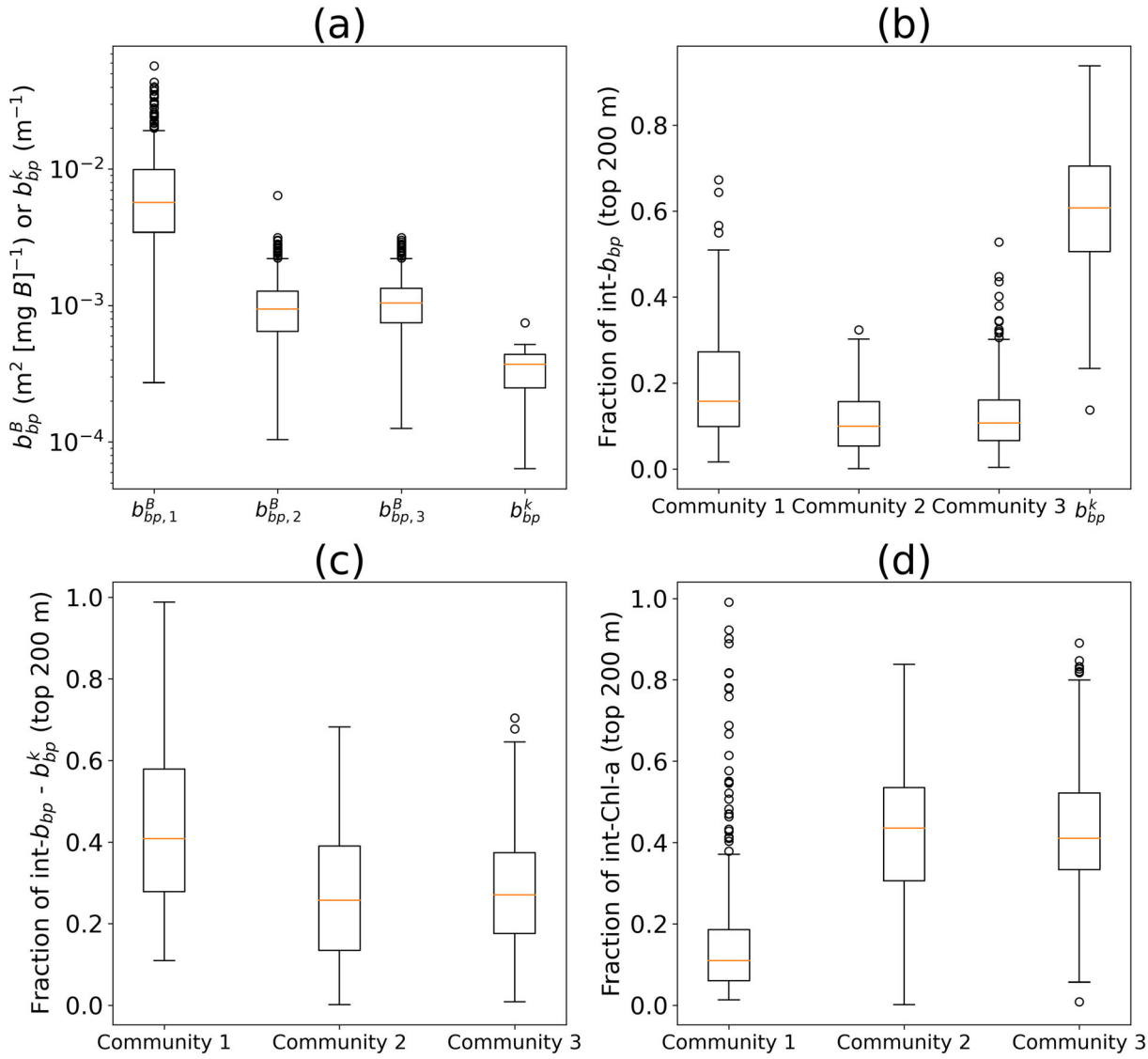

Fig. 6. Boxplots displaying (**a**) chlorophyll-specific particulate backscattering values for C_1, C_2, C_3, and the background backscattering coefficient (b_{bp}^{k}), (**b**) fractions of integrated particulate backscattering for C_1, C_2, C_3, and b_{bp}^{k}, (**c**) fractions of integrated particulate backscattering for C_1, C_2, C_3 having removed b_{bp}^{k}, (**d**) fractions of integrated Chl *a* for C_1, C_2, and C_3.

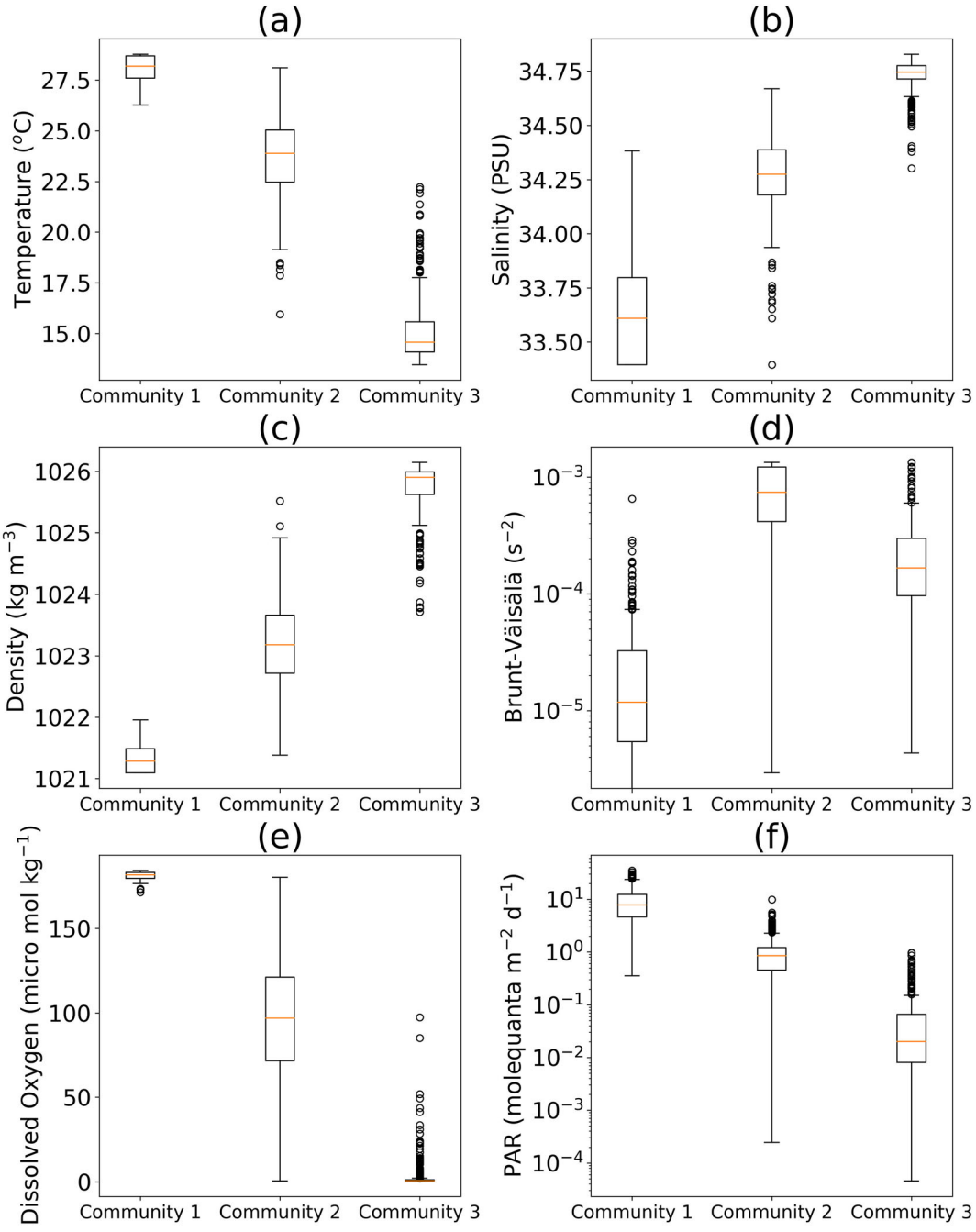

Fig. 7. Environmental conditions in which C_1, C_2, and C_3 inhabit, (**a**) temperature (°C), (**b**) salinity (PSU), (**c**) density (kg m^{-3}), (**d**) Brunt-Välsälä (s^{-2}), (**e**) DO (μmol kg^{-1}), and (**f**) PAR (mole quanta m^{-2} d^{-1}).

23.9°C), but warmer than C_3. Further below the mixed layer, at a median depth of 106 m, C_3 thrives in the coldest thermal conditions (median of 14.6°C). Therefore, C_3 has adapted to thrive at depths with cooler temperatures. Varkey et al. (2015) suggest that *Synechococcus* clades I and IV can thrive in low temperatures alongside *Prochlorococcus* low-light-adapted ecotypes.

Salinity

As with the thermal conditions surrounding C_1, C_2, and C_3, the salinity of each community is also drastically different (Fig. 7b). The low salinity (median 33.61 PSU) of C_1 coincides with higher temperature outlined in Section 2.4.1. As temperature decreases with depth (Fig. 7a), salinity increases (see Fig. 7b). C_3 resides in waters with the highest salinity (median 34.74 PSU).

Density

Outlined by differing thermal and saline levels described in Sections 2.4.1 and 2.4.2, the density of the environments in which the communities thrive are clearly separable (Fig. 7c). The low density (median 1021.29 kg m^{-3}), high temperature (median 28.2°C) and low saline (median 33.61 PSU) surface waters where C_1 resides, and the denser waters (median 1023.19 kg m^{-3}) surrounding C_2 are in contrast to the highly dense (median 1025.90 kg m^{-3}), cold (median 14.56°C), and saline (median 34.74 PSU) waters in which C_3 thrives. The strong stratification in the region, and the consequent sluggish circulation of this study site supports the formation of the vertical differences in community composition (Barnett et al., 2022).

Brunt-Väisälä

Although density increases with depth, the patterns in stability (Brunt-Väisälä) are more complex (Supporting Information Fig. S2). As expected, owing to atmosphere–ocean interactions, such as wind-generated mixing of the surface layer, C_1 resides in a turbulent mixed layer (median Brunt-Väisälä of 0.000012 s^{-2}; Fig. 7d). Interestingly, despite C_3 thriving in the densest waters, it is C_2 that resides in waters with the greatest stability (median Brunt-Väisälä of 0.00074 s^{-2}), being located at the top of the thermocline between depths of ~ 20–100 m. C_3 is found in waters with lower stability than C_2 (median Brunt-Väisälä of 0.00017 s^{-2}), because of its position below the thermocline and oxycline.

Dissolved oxygen

Atmosphere–ocean interaction and oxygen production through phytoplanktonic photosynthesis (having a greater oxygen production rate over respirational removal) places C_1 in waters with the highest DO in the water column, with a median 181.79 μmol kg^{-1} (Fig. 7e). Community respiration below the mixed layer where C_2 thrives, and lower net primary production (oxygen production), results in lower DO (median 96.63 μmol kg^{-1}). The near permanent stratification of the water column and respiration exhausts the oxygen supply at the depths in which C_3 thrives, resulting in extreme oxygen depletion with a median of 0.55 μmol kg^{-1} (this value should be interpreted with caution given how close it is to the limit of detection of the oxygen sensor) suggesting physiological adaptions of C_3 to extremely low-oxygen conditions.

Photosynthetically active radiation

At the bottom of the euphotic zone, C_3 is characterized by very low light (median of 0.02 mol quanta m^{-2} d^{-1}, acknowledging this value should be interpreted with caution given how close it is to the limit of detection of the PAR sensor, ~ 0.04% surface irradiance), resulting in a low-light adapted community (Ulloa et al. 2021). C_1 receives the highest level of light (median PAR of 7.77 mol quanta m^{-2} d^{-1} in the mixed layer, ~20% surface irradiance), due to its position at the ocean surface (Fig. 7f). The C_2 population receives around 0.85 mol quanta m^{-2} d^{-1} of PAR (~ 1.2% surface irradiance). In other words, on average the C_3 population receives light fluxes that are more than three orders of magnitude less than what phytoplankton at the very surface receive.

Discussion

Model performance and extension to three communities

The model fit

Dynamics and trends of the float data are encapsulated by the model, which was successful in detecting the presence of three communities (C_1, C_2, and C_3) in the water column (between depths of 0–200 m), demonstrating reasonable fit to the data and model performance as indicated by low residual and relative errors (Figs. 3 and 4, Supporting Information Fig. S1). The patterns in the in-situ Chl *a* data (Fig. 3a) are reflected well in the modeled Chl *a* data (Fig. 3b)—similar to the b_{bp} data in Fig. 4—with the model successfully reproducing the trends of the in-situ Chl *a* and b_{bp} data (aim 1 of this study). However, while the model fit generally captures data trends and patterns, there is a slight tendency of the model to overestimate Chl *a* above the defined peaks of C_2 and C_3 (Fig. 3c). Meanwhile, there is also an occasional slight underestimation below the peaks. In a few cases, where profiles are more complex and the three-community model fails to represent the data well, larger biases between the model and the in-situ data were observed (Fig. 3c).

The three-component model is designed to partition the vertical profiles of Chl *a* and b_{bp} into three communities of phytoplankton using Gaussian and Sigmoid functions (Brewin et al. 2022). Here, C_1 is defined by a sigmoid function, with its parameters being tied to the mixed-layer depth (Eq. 1). Both C_2 and C_3 use Gaussian functions to describe the peak value of both DCMs, the depth of the DCMs peak, and the width of the two DCMs. The mathematical functions (gaussian and sigmoid) used in our model builds on a long history in biological oceanography (see Platt and Sathyendranath 1988; Morel and Berthon, 1989; Uitz et al. 2006; Mignot et al. 2011; Brewin et al. 2017). The model also took into consideration the law of parsimony, such that we strived to minimize the complexity of the model (only having eight parameters for the Chl *a* model) while maintaining model performance (with the model on average explaining ~ 90% of the variability in a Chl *a* profile). Nonetheless, there were some cases where the model could be improved further. For example, at times we observed a slight asymmetry in the depth distribution of community 2 and 3 (sharper rise than decline as a function of depth, *see* Fig. 2). There may be scope to refine the mathematics used in the model, or investigate different weighting methods, to improve model fitting.

Following Brewin et al. (2022), our approach makes it feasible to reconcile vertical variations in two independent proxies of phytoplankton biomass, Chl *a* and b_{bp}, by simulating changes in the chlorophyll-specific particulate backscattering

of the total community with depth. However, we do assume that each community has a fixed chlorophyll-specific particulate backscatter, which may not always hold since each community can span a range of environmental conditions. Despite the model successfully capturing the dynamics of the data collected on the BGC-Argo float (WMO 3901531), caution should be taken when fitting the model to other floats and other oceanic regions (Brewin et al. 2022). As community 3 was present in all profiles, we did not consider cases where it was absent. This simplified the tuning of our model for this study. A more flexible parameterization would need to be developed to handle cases where the presence of community 3 is more sporadic, by unifying the two-community model of Brewin et al. (2022) with this three-community model. Additionally, model parameters may need to be revised for future studies, by refining the set of conditions used for model tuning in differing environments. Such consideration will need to be made in regions characterized by complex dynamics (Schneider et al. 2014; Brewin et al. 2022).

BGC-Argo float data

While there is great capacity for data collection using autonomous profiling BGC-Argo floats, there are challenges in ensuring that the data and conclusions drawn from analysis are of sufficient quality. Currently, autonomous profiling floats use Chl *a* fluorescence as a proxy of Chl *a* concentration (Barbieux et al. 2017). However, for the same Chl *a* concentration, the fluorescence yield of phytoplankton can vary depending on environment and growth conditions, and species composition (Ricour et al. 2021; Brewin et al. 2022; Martiny et al. 2022; Petit et al. 2022). Additionally, Chl *a* fluorescence is sensitive to NPQ (Xing et al. 2016). Although corrections to NPQ are part of standard BGC-Argo processing, additional work is needed to improve and validate them, as well as in the conversion of chlorophyll fluorescence into Chl *a* concentration. Poorly oxygenated waters can have high concentrations of dissolved organic matter (Loginova et al. 2020). The Chl *a* fluorescence signal can also be affected by the content and presence of colored dissolved organic matter, producing a deceptive increase in Chl *a* concentration with depth in some regions (Ricour et al. 2021). Some confidence in the data analyzed here can be gained from the general agreement in patterns of b_{bp} data and Chl *a* fluorescence data (Figs. 3 and 4). Challenges are also faced when ensuring the quality of b_{bp} data, frequently used as a proxy of the stock of POC (Barbieux et al. 2017). An example is seen in Fig. 4 showing data collected between July and August in 2018, that contained suspiciously high b_{bp} data that had to be removed from the analysis. It is therefore critical that robust protocols be established to maximize data quality and quantify data uncertainties. Future developments in BGC-Argo float design might also lead to the incorporation of detectors for measuring phytoplankton absorption in the red spectrum that will aid the estimation of Chl *a* concentration, as a compliment to fluorescence-based sensors and methods (Dall'Olmo et al. 2012; Brewin et al. 2016).

The advantage of BGC-Argo floats lies in their ability to sample the interior global ocean in a temporally and spatially continuous way, which compliments satellite data by providing information on the vertical profile of the water column. This provides the opportunity, for the first time, to study phytoplankton populations in the first and second DCM in remote locations, in a systematic manner, while being a rich source of data that can be exploited appropriately and optimally.

Vertical structure of low-oxygen-adapted phytoplankton

Thriving in poorly oxygenated water, C_3 is positioned at a depth of around 100 m (Fig. 5b). In contrast to C_1 and C_2, found between 0 and 50 m and at around 60 m respectively, there is a clear vertical partitioning of communities with depth (Figs. 3 and 4). Niche-partitioning in the vertical water column indicates differing growth and nutrient environments across communities (Scanlan et al. 2009). Such vertical partitioning is considered instrumental (Cepeda-Morales et al. 2009; Scanlan et al. 2009; Varkey et al. 2015; Thompson et al. 2021) in the development of differing *Synechococcus* and *Prochlorococcus* ecotypes and clades. In support of our findings, Goericke et al. (2000) identified a low-oxygen-adapted phytoplanktonic community—located $8 \pm 2^{\circ}$ N of this study—to thrive at 120 m. Although this depth is slightly deeper than that found in our study (Fig. 5), both studies found this community to reside slightly below the oxycline (Fig. 3 and Supporting Information Figs. S2, S4). Goericke et al. (2000) suggest that this community is dominated by low-light-adapted *Prochlorococcus* ecotypes (97% contribution to Chl *a* concentrations) with a minor presence of *Synechococcus* (< 3% of Chl *a* concentrations).

Ecological niches of C_3 typically (though not always) appear to manifest themselves with a smaller peak Chl *a* concentration (median 0.30 mg m^{-3}) when compared with the DCM where C_2 dominates (median 0.49 mg m^{-3}). The physiological and genetic adaptations required for phytoplanktonic growth at $\sim$ 100 m depths and their associated environmental constraints, such as low light (see Section 3.3), seem to reduce peak Chl *a* concentrations of the second DCM (C_3). While the peak is greater for C_2 than C_3, the width of peak (m) is greater for C_3 (by $\sim$ 11 m). Located below the mixed layer at the top of the thermocline, C_2 may have greater temperature sensitivity than C_3, characteristic of clades within the high-light-adapted *Prochlorococcus* thought to dominate in the eastern tropical North Pacific (Goericke et al. 2000).

Adaptation and composition of the low-oxygen community

The physiological response of phytoplankton to light availability is tied to depth (Khanna et al. 2005), vertical mixing (Lewis et al. 1984), and the spectral quality of available light (Sathyendranath and Platt 2007). Light availability is thought

to be an important factor controlling vertical variations in community composition (Márquez-Artavia et al. 2019). Thriving at depths of ~ 100 m, C_3 appears to be acclimated to very low light. The b_{bp} : Chl *a* ratio has been used as a proxy for the carbon : Chl *a* ratio (Brewin et al. 2022), and to understand changes in photoacclimation and photoadaption. C_3 has significantly lower chl-specific backscattering than C_1 that resides in the well-lit mixed layer (Fig. 6b). The lower b_{bp} : Chl *a* ratio of C_3 is consistent with the theoretical understanding of photoacclimation in low-light adapted phytoplankton (Sathyendranath et al. 2020; Brewin et al. 2022). With a low b_{bp} : Chl *a* ratio, C_3 is composed of low-light adapted phytoplanktonic cells, while C_1 is characterized by cells adapted to high irradiance (Sathyendranath et al. 2020), consistent with the findings of Wojtasiewicz et al. (2021), who studied the phytoplanktonic community within the second DCM in very low oxygen waters of the Arabian Sea. The physiological adaptations to light variability, to achieve optimal growth at depths, have been linked to the phylogenetic distinct clades of the cyanobacteria, *Synechococcus* and *Prochlorococcus* (Biller et al. 2015). Considering the suggested dominance of *Prochlorococcus* within the ETNP, the low chl-specific backscattering may be attributed to the community's composition of primarily low-light-adapted *Prochlorococcus* ecotypes, similar to the communities identified by Wojtasiewicz et al. (2021) in the Arabian Sea. That said, it could also be argued that differences in the chl-specific backscattering coefficients of C_1, C_2, and C_3 could also reflect the depth variation in taxonomy and size of the phytoplanktonic cells (Brewin et al. 2022). Therefore, while the b_{bp} : Chl *a* ratio is a useful tool to understand the phylogenetic adaptations and photoacclimation of naturally occurring low-light-adapted phytoplankton in the oceans, influence of species composition, taxonomy and cell structure should also be considered. Such consideration is required when comparing the chl-specific backscattering associated with C_2 and C_3. Being unexpectedly similar, despite differences in depth and environmental conditions (see Section 3.5), differences in species composition of these two low-light adapted phytoplankton communities, could be responsible for the lack of variance between them. For example, the derivation of Chl *a* from fluorescence in this work assumes no change in the slope factor (linear conversion of fluorescence to Chl *a*) with depth or community composition. Yet, variations have been observed (Petit et al. 2022), which may have masked differences in the b_{bp} : Chl *a* ratio between C_2 and C_3 in this work. Nitrogen-producing heterotrophic bacteria are also known to exist in OMZ and impact b_{bp} (Rasse et al. 2020), which may also influence the b_{bp} : Chl *a* ratio of C_3, in instances when the heterotrophic bacterial backscattering signal is not captured in the background (b_{bp}^{k}).

Importance to integrated stocks

The contribution of each community to the integrated stocks of Chl *a* and b_{bp} provides an indication of their contribution to phytoplanktonic biomass. The contribution of C_1 to integrated Chl *a* is generally low, at around 11%, though, during blooms, can be high (Fig. 3c). Compared with C_2 and C_3, C_1 has a higher contribution to integrated b_{bp}, as can be inferred from the differences in the chl-specific particulate backscattering coefficient (Fig. 6a–c, see also Fig. 4 and Supporting Information Fig. S5). The communities C_2 and C_3 contribute more to integrated stocks of Chl *a* than C_1, with roughly equal contributions of $\sim 45 \pm 4\%$ (average 44% and 41% respectively—see Fig. 6d). Yet, C_2 and C_3 contribute less than C_1 to integrated b_{bp}, with each contributing ~ 30%, compared to the ~ 40% contribution to the total from C_1, once the contribution of the background population of nonalgal particles was removed (Fig. 6c). Brewin et al. (2022) suggest that such patterns would be consistent with depth-dependant variations in the carbon : Chl *a* ratio of phytoplankton (*see* Section 3.3). The results presented here indicate C_3 to have important contributions to integrated stocks of Chl *a* (~ 41%) and b_{bp} (~ 30% after the removal of background b_{bp} values), which have implications for estimating phytoplankton stocks from satellite remote sensing, since like C_2, this community cannot be observed from space.

Habitat and environmental conditions

Through partitioning Chl *a* and b_{bp} into three communities, we have quantified differences in their environmental conditions (Fig. 7). Previous research has highlighted phytoplanktonic cells to be phylogenetically influenced—specifically through the influence on the Chl *a* : carbon ratio—by differences in oceanographic gradients, including temperature, salinity, density, oxygen, and light gradients (Sathyendranath et al. 2020; Thompson et al. 2021). At a median depth of ~ 106 m, C_3 thrives below the euphotic zone and is adapted to low irradiance (PAR around 0.02 molequanta $m^{-2} d^{-1}$, ~ 0.04% of surface irradiance), while C_1 is adapted to high light (PAR around of 7.77 molequanta $m^{-2} d^{-1}$). These adaptions are further supported by the low chl-specific backscattering of C_3. Mella-Flores et al. (2012) have demonstrated that *Prochlorococcus* and *Synechococcus* strains tune their photosynthetic apparatus to PAR fluctuations. Goericke et al. (2000) suggested that the deep and tropical populations of *Synechococcus* in the ETNP, co-existing with *Prochlorococcus* in the C_3, are physiologically inactive, and that the community is primarily dominated by low-light-adapted strains of *Prochlorococcus*. As seen in Fig. 3f, C_3 resides at DO concentrations $< 5\,\mu$mol kg^{-1}. Cepeda-Morales et al. (2009) suggested that this might be made possible by an adaptive mechanism that enables the maintenance of an aerobic metabolism in very low oxygen waters. Ulloa et al. (2021) have suggested this to be related to the supplementation of carbon and energy requirements, via organic compounds, that allows survival in dark poorly oxygenated waters, an adaptation indicated to be founded in the

evolutionary relationship between *Prochlorococcus* and oxygen availability.

Strong stratification in the ETNP is mirrored in the oxygen distribution (Supporting Information Fig. 2) within the upper 200 m of an OMZ (Garcia-Robledo et al. 2017). C_1 resides in the turbulent mixed layer, with higher oxygen concentrations (a median of 181.79 μmol kg^{-1} and a Brunt-Välsälä frequency N^2 of 0.0007 s^{-2}), between depths of 0–35 m (see Supporting Information Figs. S2, S4) where production is higher than consumption, and air-sea gas exchange occurs. The oxygen concentration surrounding C_2 deeper in the water column—at a median depth of $\sim$ 60 m—reaches values around 100 μmol kg^{-1}, as oxygen demand and respiration increases, and biomass-specific photosynthesis decreases, reducing oxygen production. Depletion of oxygen within this layer is due to heightened metabolic activity, microbial decomposition, and consumption within a stratified region (Garcio-Robledo et al. 2017; IPCC 2018). In drastic contrast to C_1 and C_2, C_3 thrives in extremely low oxygen concentrations (< 1 μmol kg^{-1}). Immediate consumption by microbial communities of oxygen produced by C_3, along with the lack of oxygen replenishment within this layer due to sluggish circulation, has been referred to as a cryptic oxygen cycle (Garcia-Robledo et al. 2017). The low irradiance and low oxygen levels where C_3 resides correspond well with previous values identified in the eastern Equatorial Pacific, and also in the poorly-oxygenated waters of the Arabian Sea, both of which are thought to be dominated by the cyanobacterium, *Prochlorococcus* (Goericke et al. 2000; Cepeda-Morales et al. 2009; Lavin et al. 2010; Garcia-Robledo et al. 2017; Marquez-Artavia et al. 2019; Ulloa et al. 2021). We extracted environmental conditions for communities 2 and 3 at the depths of their maximum abundance. Our justification for this is that these depths likely reflect their environmental niches. However, we acknowledge that their presence is not solely limited to these depths, and that these communities are observed in a range of environmental conditions centered around those at the depths of their maximum. Additionally, seasonal variability in some of these environmental conditions is expected.

Role of low-oxygen phytoplankton in a changing world

Anthropogenic climate change projections reported by the IPCC (2018) highlight the implications of rising sea-water temperatures on the ocean's oxygen inventory. A reported 2% decrease in oxygen saturation between 1960 and 2018, is projected to increase by a further 1%–7% by 2100 under all of IPCC's representative concentration pathways (Keeling et al. 2010; IPCC 2018; Long et al. 2019). Intensification of oxygen depletion in the global ocean (Stramma et al. 2008) is expected to sharpen the oxycline and cause the shoaling of OMZ into and near the euphotic depth, potentially benefitting C_3 (Long et al. 2019). The biomass of C_3—specifically that of the assumed dominant species *Prochlorococcus*—may increase as deoxygenation is enhanced globally, furthering their global importance (Agusti et al. 2019).

Future work

This work has been limited to the analysis of a single BGC-Argo float in the ETNP. Quantifying the wider distribution of this low-oxygen-adapted phytoplankton community may help our understanding of biogeochemical cycles in OMZ regions. Fitting the three-community model to multiple floats and datasets from the region (ETNP), combined with linking the parameters to larger scale environmental fields amenable to satellite remote sensing and model simulations, could provide insight into the distribution of C_3 at large scales. We have demonstrated the potential of this model to successfully capture the presence and properties of the C_3 populations; however, the limitations outlined in Section 3.1 should be considered when conducting future work and widescale application on BGC-Argo data.

Vertical partitioning achieved by this model provided an insight into C_3's contribution to integrated stocks, and a comparison with the other communities, C_1 and C_2. However, the influence of Chl *a* : biomass sensitivity (see Section 3.4), and their presence in such low-light conditions, may limit their contribution to integrated fluxes (particularly primary production). Additionally, information on the compositions of these phytoplanktonic communities, and how they may be changing, may provide insight into trophic pathways, secondary production, and trophic energy transfer (Brewin et al. 2022). Quantifying the rates of productivity of this low-light, low-oxygen adapted phytoplankton community, and their nutrient requirements, may further support our understanding on biogeochemical cycles in OMZs, while providing insights into the physiology of C_3.

Summary

A diverse array of phytoplanktonic species supports the ocean's biogeochemical cycles, occupying and thriving in a wide range of environments within the sunlit regions of the ocean. One such environment is found at the base of the euphotic zone and oxycline, within the OMZ, where a unique community of phytoplankton is known to thrive. Monitoring this deep community of phytoplankton, however, is challenging, and as a consequence, little is known about its dynamics. Here, the two-community model of Brewin et al. (2022) was extended to include a third community (C_3) that thrives in a low-light and low-oxygen environment, within the OMZ. The model was tuned to data collected by a BGC-Argo float in the ETNP. Analysis of the model and its parameters revealed the model to reproduce effectively the patterns of both Chl *a* concentrations and particulate backscattering throughout the water column. C_2 and C_3 were found to have similarly low chl-specific particulate backscattering in comparison with C_1, indicating low-light adaptation of both

communities. The low-light, low-oxygen adapted phytoplankton, C_3, is responsible for ~ 41% of integrated Chl *a* (at 200 m integration), similar to that of C_2, and ~ 30% to integrated backscattering, after accounting for background concentrations of non-algal particles, consistent with our knowledge on the depth-dependency of the carbon : Chl *a* ratio of phytoplankton. Vertical partitioning revealed drastic differences in environmental conditions between where these three communities reside, within the water column. Our results emphasize how robotic platforms such as BGC-Argo floats can be utilized to observe unique phytoplanktonic communities that thrive in extremities, and that are otherwise distinctively challenging to observe and monitor. The combination of the BGC-Argo data and simple conceptual models can be used successfully to extract characteristics of these communities. Gaining an understanding of their composition and dynamics will provide an insight into the future of the marine ecosystem under incessant anthropogenic climate change.

Data availability statement

These data were collected and made freely available by the International Argo Program and the national programs that contribute to it (https://argo.ucsd.edu, https://www.ocean-ops.org). The Argo Program is part of the Global Ocean Observing System. All data and code used in the article are provided openly on a GitHub page (https://github.com/rjbrewin/Three-community-phyto-model). This includes an example Jupyter Notebook Python Script, processing this BGC-Argo float and tuning the models.

References

Agusti, S., L. M. Lubián, E. Moreno-Ostos, A. Estrada, and C. M. Duarte. 2019. Projected changes in photosynthetic picoplankton in a warmer Subtropical Ocean. Front. Mar. Sci. **5**: 506. doi:10.3389/fmars.2018.00506

Argo. 2000. Argo float data and metadata from global data assembly Centre (Argo GDAC). SEANOE. doi:10.17882/42182

Arrigo, K. R. 2005. Marine microorganisms and global nutrient cycles. Nature **437**: 349–355. doi:10.1038/nature04159

Barbieux, M., and others. 2017. Assessing the variability in the relationship between the particulate backscattering coefficient and the chlorophyll *a* concentration from a global biogeochemical-Argo database. J. Geophys. Res. Oceans. **123**: 1229–1250. doi:10.1002/2017JC013030

Barnett, M. L., A. E. S. Kemp, W. A. M. Nimmo-Smith, and D. A. Purdie. 2022. Total water column analysis shows the importance of a single species in subsurface chlorophyll maximum thin layers in stratified waters. Front. Mar. Sci. **8**: 733799. doi:10.3389/fmars.2021.733799

Basu, S., and K. R. M. Mackey. 2018. Phytoplankton as key mediators of the biological carbon pump: Their responses to a changing climate. Sustainability **10**: 869. doi:10.3390/su10030869

Biller, S. J., P. M. Berube, D. Lindell, and S. W. Chisholm. 2015. *Prochlorococcus*: The structure and function of collective diversity. Nat. Rev. Microbiol. **13**: 13–27. doi:10.1038/nrmicro3378

Bittig, H. C., and others. 2019. A BGC-Argo guide: Planning, deployment, data handling and usage. Front. Mar. Sci. **6**: 502. doi:10.3389/fmars.2019.00502

Bouman, H. A., and others. 2006. Oceanographic basis of the global surface distribution of *Prochlorococcus* ecotypes. Science **312**: 918–921. doi:10.1126/science.1122692

Brewin, R. J. W., G. Dall'Olmo, S. Sathyendranath, and N. J. Hardman-Mountford. 2012. Particle backscattering as a function of chlorophyll and phytoplankton size structure in the open-ocean. Opt. Express **20**: 17632–17652. doi:10.1364/OE.20.017632

Brewin, R. J. W., G. Dall'Olmo, S. Pardo, V. van Dongen-Vogels, and E. S. Boss. 2016. Underway spectrophotometry along the Atlantic meridional transect reveals high performance in satellite chlorophyll retrievals. Remote Sens. Environ. **183**: 82–97. doi:10.1016/j.rse.2016.05.005

Brewin, R. J. W., G. H. Tilstone, T. Jackson, T. Cain, P. Miller, P. K. Lange, A. Misra, and R. Airs. 2017. Modelling size-fractionated primary production in the Atlantic Ocean from remote sensing. Prog. Oceanogr. **158**: 130–149. doi:10.1016/j.pocean.2017.02.002

Brewin, R. J. W., and others. 2020. Comparison of two methods for measuring sea surface temperature when surfing. Oceans **1**: 6–26. doi:10.3390/oceans1010002

Brewin, R. J. W., and others. 2021. Sensing the ocean biological carbon pump from space: A review of capabilities, concepts, research gaps and future developments. Earth Sci. Rev. **217**: 103604. doi:10.1016/j.earscirev.2021.103604

Brewin, R. J. W., and others. 2022. A conceptual approach to partitioning a vertical profile of phytoplankton biomass into contributions from two communities. J. Geophys. Res. Oceans. **127**: e2021JC018195. doi:10.1029/2021JC018195

Cepeda-Morales, J., E. Beier, G. Gaxiola-Castro, M. F. Lavin, and V. M. Godínez. 2009. Effect of the oxygen minimum zone on the second chlorophyll maximum in the eastern tropical Pacific off Mexico. Cienc. Mar. **35**: 389–403. doi:10.7773/cm.v35i4.1622

Chai, F., and others. 2020. Monitoring ocean biogeochemistry with autonomous platforms. Nat. Rev. Earth. **1**: 315–326. doi:10.1038/s43017-020-0053-y

Claustre, H., K. S. Johnson, and Y. Takeshita. 2020. Observing the global ocean with biogeochemical-Argo. Ann. Rev. Mar. Sci. **23-48**: 23–48. doi:10.1146/annurev-marine-010419-010956

Dall'Olmo, G., E. Boss, M. J. Behrenfeld, and T. K. Westberry. 2012. Particulate optical scattering coefficients along an Atlantic meridional transect. Opt. Express **20**: 21532–21551. doi:10.1364/OE.20.021532

Duteil, O., A. Oschlies, and C. W. Böning. 2018. Pacific decadal oscillation and recent oxygen decline in the eastern tropical Pacific Ocean. Biogeosciences. **15**: 7111–7126. doi:10.5194/bg-15-7111-2018

Falkowski, P. 2012. Ocean science: The power of plankton. Nature **283**: S17–S20. doi:10.1038/483S17a

Fenchel, T., G. M. King, and T. H. Blackburn. 2012. The water column, p. 67–88. *In* T. Fenchel, G. M. King, and T. H. Blackburn [eds.], Bacterial biogeochemistry, 3rd ed. Elsevier Ltd..

Fiedler, P. C., and L. D. Talley. 2006. Hydrography of the eastern tropical Pacific: A review. Prog. Oceanogr. **69**: 2–4. doi:10.1016/j.pocean.2006.03.008

Field, C. B., M. J. Behrenfeld, J. T. Randerson, and P. Falkowski. 1998. Primary production of the biosphere: Integrating terrestrial and oceanic components. Science **281**: 237–240. doi:10.1126/science.281.5374.237

Fuchsman, C. A., and others. 2019. Cyanobacteria and cyanophage contributions to carbon and nitrogen cycling in an oligotrophic oxygen-deficient zone. ISME J. **13**: 2714–2726. doi:10.1038/s41396-019-0452-6

Garcia-Robledo, E., C. C. Padilla, M. Aldunate, F. J. Stewart, O. Ulloa, A. Paulmier, G. Gregori, and N. P. Revsbech. 2017. Cryptic oxygen cycling in anoxic marine zones. Proc. Natl. Acad. Sci. U. S. A. **114**: 8319–8324. doi:10.1073/pnas.1619844114

GCOS. 2011. Systematic observation requirements from satellite-based data products for climate (Technical Report). World Meteorological Organisation (WMO).

Goericke, R., R. J. Olson, and A. Shalapyonok. 2000. A novel niche for Prochlorococcus sp. in low-light suboxic environments in the Arabian Sea and the eastern tropical North Pacific. Deep Sea Res. Part I Oceanogr. Res. Pap **47**: 1183–1205. doi:10.1016/S0967-0637(99)00108-9

Gordon, H. R., D. K. Clark, J. L. Mueller, and W. A. Hovis. 1980. Phytoplankton pigments from the Nimbus-7 coastal zone color scanner: Comparisons with surface measurements. Science **210**: 63–66. doi:10.1126/science.210.4465.63

Groom, S., and others. 2019. Satellite Ocean colour: Current status and future perspective. Front. Mar. Sci. **6**: 485–430. doi:10.3389/fmars.2019.00485

Holte, J., and L. Talley. 2009. A new algorithm for finding mixed layer depths with applications to Argo data and subantarctic mode water formation. J. Atmos. Oceanic Tech. **26**: 1920–1939. doi:10.1175/2009JTECHO543.1

IOCCG. 2014. Phytoplankton functional types from space. *In* S. Sathyendranath [ed.], Reports of the International Ocean-colour coordinating group, v. **15**. IOCCG.

IPCC. 2018. An IPCC special report on the impacts of global warming of 1.5°C above pre-industrial levels and related global greenhouse gas emission pathways, in the context of strengthening the global response to the threat of climate change, sustainable development, and efforts to eradicate poverty, p. 616. *In* V. Masson-Delmotte and others [eds.], Global warming of 1.5°C. Cambridge University Press. doi:10.1017/9781009157940

Keeling, R. F., A. Körtzinger, and N. Gruber. 2010. Ocean deoxygenation in a warming world. Ann. Rev. Mar. Sci. **2**: 199–229. doi:10.1146/annurev.marine.010908.163855

Khanna, D. R., R. Bhutiani, and K. S. Chandra. 2005. Modelling the effect of light on phytoplanktonic growth dynamics: A review. Environ. Conserv. J. **6**: 103–107. doi:10.36953/ECJ.2005.0612315

Lam, P., and M. M. M. Kuypers. 2011. Microbial nitrogen cycling processes in oxygen minimum zones. Ann. Rev. Mar. Sci. **3**: 317–345. doi:10.1146/annurev-marine-120709-142814

Lavin, P., B. González, J. F. Santibáñez, D. J. Scanlan, and O. Ulloa. 2010. Novel lineages of *Prochlorococcus* thrive within the oxygen minimum zone of the eastern tropical South Pacific. Environ. Microbiol. Rep. **2**: 728–738. doi:10.1111/j.1758-2229.2010.00167.x

Le Quéré, C., and others. 2005. Ecosystem dynamics based on plankton functional types for global ocean biogeochemistry models. Glob. Chang. Biol. **11**: 2016–2040. doi:10.1111/j.1365-2486.2005.1004.x

Lewis, M. R., J. J. Cullen, and T. Platt. 1984. Relationships between vertical mixing and photoadaptation of phytoplankton: Similarity criteria. Mar. Ecol. Prog. Ser. **15**: 141–149.

Loginova, A. N., A. W. Dale, F. A. C. Le Moigne, S. Thomsen, S. Sommer, D. Clemens, K. Wallmann, and A. Engel. 2020. Sediment release of dissolved organic matter to the oxygen minimum zone off Peru. Biogeosciences. **17**: 4663–4679. doi:10.5194/bg-17-4663-2020

Long, M. C., T. Ito, and C. Deutsch. 2019. Oxygen projections for the future. *In* D. Laffoley and J. M. Baxter [eds.], Ocean deoxygenation: Everybody's problem. IUCN.

Longhurst, A., S. Sathyendranath, T. Platt, and C. Caverhill. 1995. An estimate of global primary production in the ocean from satellite radiometer data. J. Plankton Res. **17**: 1245–1271. doi:10.1093/plankt/17.6.1245

Marañón, E. 2009. Phytoplankton size and structure, p. 4249–4256. *In* J. H. Steele, S. A. Thorpe, and K. K. Turekian [eds.], Encyclopedia of ocean sciences, 2nd ed. Academic Press. doi:10.1016/B978-012374473-9.00661-5

Márquez-Artavia, A., L. Sánchez-Velasco, E. D. Barton, A. Paulmier, E. Santamariá-Del-Ángel, and E. Beier. 2019. A suboxic chlorophyll-a maximum persists within the Pacific oxygen minimum zone off Mexico. Deep Sea Res. Part II: Top. Stud. Oceanogr. 169–170: 1–8. doi:10.1016/j.dsr2.2019.104686

Martiny, A. C., and others. 2022. Marine phytoplankton resilience may moderate oligotrophic ecosystem responses and biogeochemical feedbacks to climate change. Limnol. Oceanogr. **67**: S378–S389. doi:10.1002/lno.12029

Mella-Flores, D., and others. 2012. *Prochlorococcus* and *Synechococcus* have evolved different adaptive mechanisms to

cope with light and UV stress. Front. Microbiol. **3**: 285. doi:10.3389/fmicb.2012.00285

Mignot, A., H. Claustre, F. d'Ortenzio, X. Xing, A. Poteau, and J. Ras. 2011. From the shape of the vertical profile of in vivo fluorescence to chlorophyll-a concentration. Biogeosciences **8**: 2391–2406. doi:10.5194/bg-8-2391-2011

Moisan, T. A., K. M. Rufty, J. R. Moisan, and M. A. Linkswiler. 2017. Satellite observations of phytoplankton functional type spatial distributions, phenology, diversity, and ecotones. Front. Mar. Sci. **4**: 189. doi:10.3389/fmars.2017.00189

Morel, A., and J. F. Berthon. 1989. Surface pigments, algal biomass profiles, and potential production of the euphotic layer: Relationships reinvestigated in view of remote-sensing applications. Limnol. Oceanogr. **34**: 1545–1562. doi:10.4319/lo.1989.34.8.1545

Petit, F., and others. 2022. Influence of the phytoplankton community composition on the in situ fluorescence signal: Implication for an improved estimation of the chlorophyll-a concentration from BioGeoChemical-Argo profiling floats. Front. Mar. Sci. **9**: 959131. doi:10.3389/fmars.2022.959131

Platt, T., and S. Sathyendranath. 1988. Oceanic primary production: Estimation by remote sensing at local and regional scales. Science **241**: 1613–1620. doi:10.1126/science.241.4873.1613

Rasse, R., H. Claustre, and A. Poteau. 2020. The suspended small-particle layer in the oxygen-poor Black Sea: A proxy for delineating the effective N_2-yielding section. Biogeosciences **17**: 6491–6505. doi:10.5194/bg-17-6491-2020

Ravichandran, M., M. S. Girishkumar, and S. Riser. 2012. Observed variability of chlorophyll-a using Argo profiling floats in the southeastern Arabian Sea. Deep Sea Res. Part I Oceanogr. Res. Pap **65**: 15–25. doi:10.1016/j.dsr.2012.03.003

Reynolds, C. S. 2006. Ecology of phytoplankton. Cambridge University Press.

Ricour, F., A. Capet, F. D'Ortenzio, B. Delille, and M. Grégoire. 2021. Dynamics of the deep chlorophyll maximum in the Black Sea as depicted by BGC-Argo floats. Biogeosciences. **18**: 755–774. doi:10.5194/bg-18-755-2021

Roesler, C., and others. 2017. Recommendations for obtaining unbiased chlorophyll estimates from in situ chlorophyll fluorometers: A global analysis of WET labs ECO sensors. Limnol. Oceanogr. Methods. **15**: 572–585. doi:10.1002/lom3.10185

Sathyendranath, S., and T. Platt. 2007. Spectral effects in bio-optical control on the ocean system. Oceanologia. **49**: 5–39.

Sathyendranath, S., and others. 2019. An ocean-colour time series for use in climate studies: The experience of the ocean-colour climate change initiative (OC-CCI). Sensors. **19**: 4285. doi:10.3390/s19194285

Sathyendranath, S., and others. 2020. Reconciling models of primary production and photoacclimation. Appl. Optics **59**: C100–C114. doi:10.1364/AO.386252

Scanlan, D. J., and others. 2009. Ecological genomics of marine Picocyanobacteria. Microbiol. Mol. Biol. Rev. **73**: 249–299. doi:10.1128/MMBR.00035-08

Schmechtig, C., H. Claustre, A. Poteau, and F. D'Ortenzio. 2018. Bio-Argo quality control manual for chlorophyll-A concentration version 1.1. Ifremer.

Schmechtig, C., E. Boss, N. Briggs, H. Claustre, G. Dall'Olmo, and A. Poteau. 2019. BGC Argo quality control manual for particles backscattering. Ifremer. doi:10.13155/60262

Schneider, T., T. Bischoff, and G. H. Haug. 2014. Migrations and dynamics of the intertropical convergence zone. Nature **513**: 45–53. doi:10.1038/nature13636

Stramma, L., G. C. Johnson, J. Sprintall, and V. Mohrholz. 2008. Expanding oxygen-minimum zones in the tropical oceans. Science **320**: 655–658. doi:10.1126/science.1153847

Stramma, L., G. C. Johnson, E. Firing, and S. Schmidtko. 2010. Eastern Pacific oxygen minimum zones: Supply paths and multidecadal changes. J. Geophys. Res. Oceans. **115**: 1–12. doi:10.1029/2009JC005976

Thompson, A. W., K. Kouba, and N. A. Ahlgren. 2021. Niche partitioning of low-light adapted *Prochlorococcus* subecotypes across oceanographic gradients of the North Pacific subtropical front. Limnol. Oceanogr. **66**: 1548–1562. doi:10.1002/lno.11703

Tiano, L., E. Garcia-Robledo, T. Dalsgaard, A. H. Devol, B. B. Ward, O. Ulloa, D. E. Canfield, and N. P. Revsbech. 2014. Oxygen distribution and aerobic respiration in the north and south eastern tropical Pacific oxygen minimum zones. Deep Sea Res. Part I Oceanogr. Res. Pap **94**: 173–183. doi:10.1016/j.dsr.2014.10.001

Timmermann, A., and F.-F. Jin. 2002. Phytoplankton influences on tropical climate. Geophys. Res. Lett. **29**: 191–194. doi:10.1029/2002GL015434

Uitz, J., H. Claustre, A. Morel, and S. B. Hooker. 2006. Vertical distribution of phytoplankton communities in open ocean: An assessment based on surface chlorophyll. J. Geophys. Res. Oceans **111**: 1–23. doi:10.1029/2005JC003207

Ulloa, O., D. E. Canfield, E. F. DeLong, R. M. Letelier, and F. J. Stewart. 2012. Microbial oceanography of anoxic oxygen minimum zones. Proc. Natl. Acad. Sci. U. S. A. **109**: 15996–16003. doi:10.1073/pnas.1205009109

Ulloa, O., C. Henríquez-Castillo, S. Ramírez-Flandes, A. M. Plominsky, A. A. Murillo, C. Morgan-Lang, S. J. Hallam, and R. Stepanauskas. 2021. The cyanobacterium Prochlorococcus has divergent light-harvesting antennae and may have evolved in a low-oxygen ocean. Proc. Natl. Acad. Sci. U. S. A. **118**: e2025638118. doi:10.1073/pnas.2025638118

Varkey, D., S. Mazard, M. Ostrowski, S. G. Tetu, P. Haynes, and I. T. Paulsen. 2015. Effects of low temperature on tropical and termperate isolates of marine *Synechococcus*. ISME J. **10**: 1–12. doi:10.1038/ismej.2015.179

Wojtasiewicz, B., and others. 2021. Autonomous profiling float observations reveal the dynamics of deep biomass

distributions in the denitrifying oxygen minimum zone of the Arabian Sea. J. Mar. Syst. **207**: 103103. doi:10.1016/j.jmarsys.2018.07.002

Whitmarsh, F., J. Zika, and A. Czaja. 2015. Ocean heat uptake and the global surface temperature record. Grantham Institute Briefing Paper, 14. Imperical College London, September 2015.

Whitmire, A. L., R. M. Letelier, V. Villagrán, and O. Ulloa. 2009. Autonomous observations of in vivo fluorescence and particle backscattering in an oceanic oxygen minimum zone. Opt. Express **17**: 21992–22004. doi:10.1364/OE.17.021992

Xing, X., H. Claustre, S. Blain, F. D'Ortenzio, D. Antoine, J. Ras, and C. Guinet. 2012. Quenching correction for in vivo chlorophyll fluorescence acquired by autonomous platforms: A case study with instrumented elephant seals in the Kerguelen region (Southern Ocean). Limnol. Oceanogr. Methods. **10**: 483–495. doi:10.4319/lom.2012.10.483

Xing, X., H. Claustre, E. Boss, C. Roesler, E. Organelli, A. Poteau, M. Barbieux, and F. D'Ortenzio. 2016. Correction of profiles of in-situ chlorophyll fluorometry for the contribution of fluorescence originating from non-algal matter. Limnol. Oceanogr. Methods. **15**: 80–93. doi:10.1002/lom3.10144

Zhang, X., L. Hu, Y. Xiong, Y. Huot, and D. Gray. 2020. Experimental estimates of optical backscattering associated with submicron particles in clear oceanic waters. Geophys. Res. Lett. **47**: e2020GL087100. doi:10.1029/2020GL087100

Acknowledgments

We acknowledge all those involved in the deployment and of the BGC-Argo float (WMO number 3901531) used in the study. This work was supported by a UKRI Future Leader Fellowship (MR/V022792/1); the European Space Agency (ESA) project Biological Pump and Carbon Exchange Processes (BICEP); by the Simons Foundation Project Collaboration on Computational Biogeochemical Modeling of Marine Ecosystems (CBIOMES; 549947, SS); and by the Royal Society, in the framework of the Newton International Fellowship (grant NF150203). Isabelle Cox was supported by a MSc in Marine Vertebrate Ecology and Conservation, in the College of Life and Environmental Sciences, and a PhD studentship in the Centre for Geography and Environmental Science, both at the University of Exeter. GDO has received funding from the European Union's Horizon 2020 research and innovation programme under grant agreement No 862923. This output reflects only the author's view and the European Union cannot be held responsible for any use that may be made of the information contained therein. We thank the editors, Ricardo M Letelier and one anonymous reviewer for useful comments on our manuscript that helped us significantly improve it.

Conflict of Interest

None declared.

Submitted 16 December 2022
Revised 16 May 2023
Accepted 28 June 2023

Associate editor: David Antoine